2025 26th International Conference on Thermal, Mechanical and Multi-Physics Simulation and Experiments in Microelectronics and Microsystems (EuroSimE) | 979-8-3503-9300-2/25/$31.00 ©2025 IEEE | DOI: 10.1109/EUROSIME65125.2025.11006620

Multiphysics Modeling of a Novel MEMS Accelerometer Based on Electromagnetic Induction

Ozberk Ozturk
Faculty of Engineering and Natural Sciences
Sabanci University
Istanbul, Türkiye
ozberk@sabanciuniv.edu

Fares Tounsi
ICTEAM Institute
UCLouvain
Louvain-la-Neuve, Belgium
fares.tounsi@uclouvain.be

Laurent Francis
ICTEAM Institute
UCLouvain
Louvain-la-Neuve, Belgium
laurent.francis@uclouvain.be

Denis Flandre
ICTEAM Institute
UCLouvain
Louvain-la-Neuve, Belgium
denis.flandre@uclouvain.be

Murat Kaya Yapici
Faculty of Engineering and Natural Sciences
Sabanci University, Istanbul, Türkiye
Department of Electrical and Computer Engineering,
University of Washington, Seattle, USA
murat.yapici@sabanciuniv.edu

***Abstract*—This work reports on the development of a micromachined monolithic single-axis electromagnetic accelerometer based on the relative motion between the windings of a concentric planar transformer, whose internal inductor is suspended. The mechanical and electromagnetic modelling of the sensor is presented, as well as the implementation of a virtual read-out circuit. Electromagnetic simulations were used to extract the electrical performance parameters in the form of a lumped-element model. The results demonstrate that rotation between the two windings leads to an approximately linear variation in the mutual inductance. Furthermore, measurement circuit simulations revealed that the sensor could achieve an in-plane acceleration sensitivity of 32.9 mV/g for a matched network when excited with 3V$_{pp}$, 100 MHz excitation voltage.**

Keywords—inductive accelerometer, MEMS, micromachined, electromagnetic induction, on-chip transformer.

I. Introduction

Microelectromechanical systems (MEMS) technology enables the integration of mechanical and electrical components at a microscopic scale to achieve integrated devices and systems. The integration of different sensing principles such as piezoelectric, piezoresistive, and capacitive into MEMS systems has enabled the creation of various families of sensors. These sensors are typically used to detect mechanical changes such as pressure and motion. As one of the earliest commercial successes of microfabrication technology, MEMS-based accelerometers are widely used for acceleration sensing and in inertial measurement units (IMUs) for a variety of applications ranging from the automotive industry to aerospace and consumer electronics [1], particularly for airbag safety, safety belt tighteners, burglar alarms, balance sensors, gaming consoles, video cameras, and navigation [2-6].

Advances in recent years indicate that the sensitivity of MEMS accelerometers could potentially reach the level of seismic monitoring for detecting underground resources (oil and natural gas) or detecting gravitational waves [7-11]. In the literature, there are examples of MEMS-based accelerometers operating under various physical sensing principles, such as capacitive, piezoelectric, piezoresistive, tunnel, optical, and others. Of these, capacitive accelerometers are the most common and commercially successful. They feature good DC response, low thermal sensitivity, and high noise tolerance. Despite their many advantages, capacitive accelerometers require complex manufacturing processes, readout circuits, and packaging [12].

Piezoresistive accelerometers, thanks to their simple fabrication and readout mechanisms, enable faster manufacturing cycle times [13]. However, they are sensitive to temperature and assembly stress, which compromises their performance and reliability. Piezoelectric accelerometers offer better temperature sensitivity, better long-term stability, and a better dynamic acceleration bandwidth than the previous two types [14]. However, integrating piezoelectric materials into the microfabrication process is not easy, and thin-film properties exhibit significant differences compared to reported values of their bulk counterparts. Furthermore, materials with high piezoelectric coefficients, such as lead zirconate titanate (PZT), are not amenable to integration into the CMOS fabrication process. Although piezoelectric devices have the potential to operate as self-powered systems, this functionality is limited to scenarios involving dynamic acceleration inputs. This means that piezoelectric accelerometers are generally suitable for applications such as vibration monitoring where the operating bandwidth is high. Research into tunneling and optical accelerometers is also promising, providing highly sensitive sensors with a small form factor, but to date, sensors operating with these principles have not been commercialized.

As an alternative sensing mechanism, the electromagnetic transduction principle has not yet been widely studied, although it has been briefly mentioned in a few studies [15, 16]. No accurate MEMS-based electromagnetic accelerometer has yet been developed to the level where it can be utilized in a practical application setting. This type of accelerometer would rely on inductive coupling between two inductors, where the relative motion or mechanical change between the two coils is directly translated into a variation in the induced voltage, resulting in a simple read-out circuit. The microfabrication of this sensor would also resemble that of planar, on-chip concentric transformers, enabling seamless CMOS-compatible monolithic integration with readout ICs. In this paper, we present a comprehensive multi-physics model of the proposed inductive accelerometer based on the electromagnetic transduction principle. The following sections describe the mechanical design of the accelerometer, extraction of its electrical parameters, the inductive coupling

between the two inductors, and the evaluation of its performance through simulation of the read-out circuitry.

II. Methodology

The proposed design of the electromagnetic accelerometer is based on generating relative motion between two planar inductors of a concentric planar transformer (Fig. 1a). The basic idea is to design a monolithic on-chip transformer, consisting of two inductors, one placed on a vibrating proof mass, while the other is placed on a fixed substrate. By subjecting the internal, mechanically free inductor (secondary) of the transformer to relative motion while exciting the external fixed inductor (primary), the induced voltage at the secondary varies proportionally to the variations in the flux linkage.

Based on this concept, a mechanical arrangement is proposed in which the moving part of the sensor is anchored to the main body by means of two torsional beams centered in the middle, resembling a seesaw (Fig. 1b). These two beams support a plate with two identical proof masses placed underneath, on the left and right. Under horizontal acceleration, symmetrical torque and angular rotation are observed on both sides. The out-of-plane rotation between the inner and outer windings decreases the inductive coupling in-between due to an increased separation distance of the adjacent metal tracks of the primary and the secondary inductors, resulting in lower mutual inductance.

III. Mechanical Design and Dimensions

The mechanical motion of the system under acceleration can be characterized by analyzing the deformation of the proof mass around the torsion beams (Fig. 1b). Under in-plane acceleration, the proof masses experience a force in opposite direction, in accordance with Newton's second law. This creates a torque at the upper surface of the proof masses, causing the plate supporting them to rotate. Applying Hooke's law for torsion and neglecting the damping effect of air, the relationship between in-plane acceleration (a) and bending angle (θ) can be written as:

$$\tau = \frac{FH}{2} = \frac{m_p a H}{2} \cong k\,\theta \quad (1)$$

where H and m_p are, respectively, the height and mass of each proof mass, and k is the torsional spring constant of the plate. Additionally, at the center of the plate, the torsion beams experience the induced shear stress and rotate according to:

$$\Phi = \frac{T\,L}{2JG} \quad (2)$$

where Φ, T, L, J, and G are, respectively, the rotation angle, torque, length of the beam, torsional moment of inertia, and shear modulus of elasticity [17]. The proof mass and the carrying plate can be optimized to improve the torque transfer. Similarly, the torsional moment of inertia, governed by the beam's cross-sectional geometry and beam length, can be adjusted to maximize rotation. Although a longer torsion beam improves the rotation angle, it creates a trade-off by reducing the coupling between the inner and outer windings. Therefore, it is more effective to design the geometry so that rotation comes from plate bending (θ) while keeping the windings close together with a shorter torsion beam length.

With these design specifications in mind, the mechanical design of the sensor was simulated and optimized in the "Solid Mechanics" module of COMSOL Multiphysics. The sensor substrate was made of 600 µm-thick monocrystalline silicon with a Young's modulus (E) of 170 GPa, while the middle plate and the torsion beams were made of 2 µm-thick silicon dioxide with E = 70 GPa. The length of the torsion beams was chosen to be 20 µm to achieve a short and realistic distance between the windings, and its width was set to 80 µm.

After choosing the plate length and plate width (L_p = 1710 µm and W_p = 650 µm), the length of the proof masses (L) must be specified. In the suggested mechanical model of the sensor, an increase in L reduces the length of the plate, creating a trade-off between the effects of the proof mass (m_p) and the spring stiffness (k) for the plate rotation. A parametric sweep study was conducted on the length of the proof mass (L) to optimize the mechanical sensitivity to acceleration as much as possible, where L was scanned between 200 and 600 µm in 50 µm steps while keeping the height (H) and width (W_p) constant (Table 1). Structural mechanic simulations were performed for twelve different geometries under an acceleration of 5g in the x-direction. The results showed two maxima at 350 µm and 500 µm. The 350 µm was preferred as it achieves the same displacement with less load on the torsional beam anchors.

Based on structural mechanics simulation, the maximum Von Mises stress on the torsion beams was estimated to be 92.3 Mpa at 5g. This figure is lower than the fracture toughness values previously reported for silicon dioxide thin

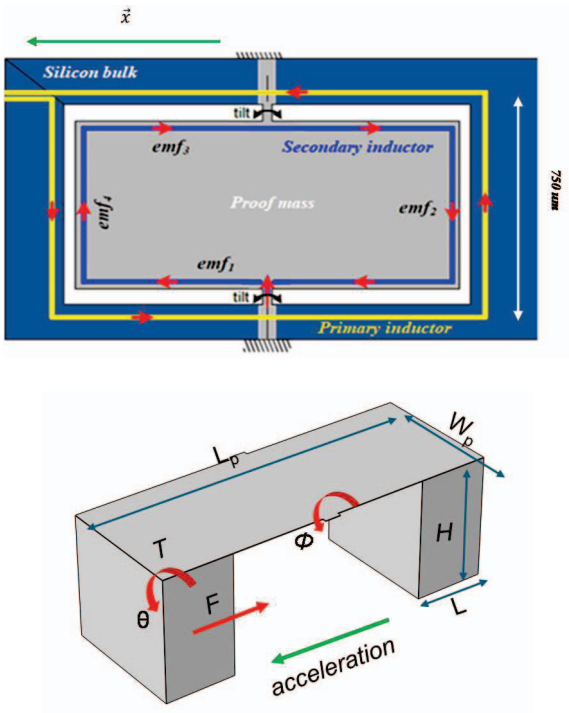

Fig. 1. An illustration of a concentric planar transformer: (a) the arrangement of the two planar inductors, where blue indicates the internal windings and yellow the external windings, and (b) the moving part of the sensor that consists in a thin plate anchored by means of two lateral torsion beams, with 2 proof masses located symmetrical at the longitudinal edges of the plate.

TABLE I. Proof mass length versus z-displacement and rotation (Θ) for 5g acceleration in the x-direction.

L (µm)	300	350	400	450	500	550	600
z (µm)	36	45	44	45	38	45	38.7
θ (°)	2.4	3.03	2.9	2.96	3.05	2.6	2.59

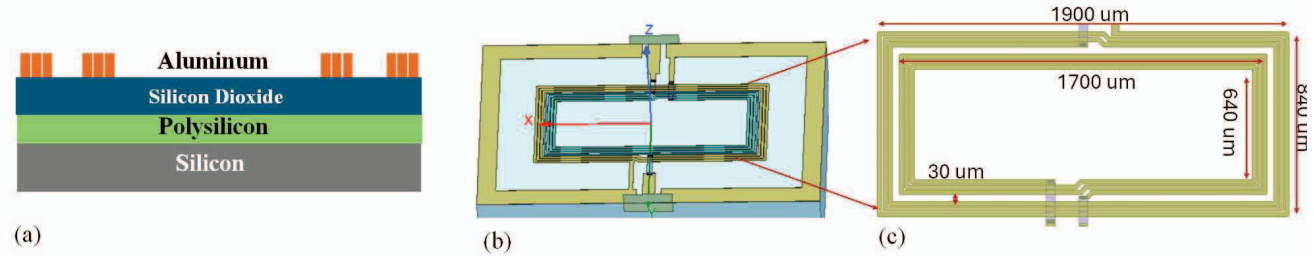

Fig. 2. Accelerometer design: (a) the material stack used in the electromagnetic simulations, (b) three-dimensional view of the sensor concept, and (c) the dimensions of the two windings.

films, indicating that the sensor design is mechanically robust [18, 19].

IV. Lumped-element extraction

The electromagnetic behavior of the proposed sensor mainly depends on the arrangement of the inner and outer inductors, as well as the surrounding material properties. The metal inductors were made of 1.8 µm thick aluminum with a bulk conductivity of 1.532 10^6 S/m, while the high resistivity silicon substrate had a relative permittivity of $\varepsilon = 11.9$ and a bulk conductivity of $\sigma = 0.02$ S/m. A 0.5 µm polysilicon layer ($\varepsilon = 11.8$, $\sigma = 0.01$ S/m) was also added to mitigate parasitic surface charges between the high resistivity silicon and the insulating silicon dioxide layers ($\varepsilon = 4$) (Fig 2a). This trap-rich layer reduces substrate losses and improves the quality factor of the inductors [20]. The inductors were arranged in three turns for the inner and outer windings, with each track 20 µm wide and 5 µm spacing between adjacent tracks (Fig. 2b). The rectangular circumference of the inner inductor was 1700 µm × 640 µm, surrounded by the outer inductor with a 30 µm spacing between them (Fig. 2c).

The electrical parameters of the sensor can be expressed by a lumped-element model used for planar inductors and transformers [21]. Fig. 3a illustrates the two-port modelling of an on-chip inductor, where the self-inductance (L), series resistance (R), and capacitance (C) are combined with the parasitic substrate capacitance (C_s), resistance (R_s), and oxide capacitance (C_{ox}) at the first and the second ports. This model can be extended to the case of an on-chip planar transformer by considering the magnetic and capacitive couplings between the two inductors using the mutual inductance (M) and the interwinding capacitance (C_i), as shown in Fig. 3b.

The electrical network parameters (S-parameters) of the two-port system were obtained using Ansys HFSS high-frequency analysis, allowing the calculation of the mutual inductance and the coupling coefficient between the two windings (Fig. 4). The configuration of the HFSS modal solutions consisted of a frequency sweep between 10 kHz and 20 GHz with an adaptive pass of $\Delta S = 0.02$. For parameter extraction, besides the two-port simulation of the complete transformer (Fig. 4a), the inner and outer windings were simulated one by one (Fig. 4b-c), as well as without a substrate to calculate the effect of substrate losses (Fig. 4d). In addition, open and short dummies were simulated and employed to de-embed the network parameters of each structure. This method allowed us to exclude the influence of the ground plane and the waveguide on the parameter extraction. For each winding, the self-inductance, series resistance, and self-capacitance values are calculated with:

$$L = \frac{\Im(Z_{11})}{\omega} \tag{3}$$

$$R = \Re(Z_{11}) \tag{4}$$

$$C = \frac{1}{(L\,\omega_{res}^2)} \tag{5}$$

where ω_{res} is the angular resonance frequency. The mutual inductance and coupling coefficient are given by:

$$M = \frac{\Im(Z_{12})}{\omega} \tag{6}$$

$$k = \frac{|M|}{\sqrt{L_1 L_2}} \tag{7}$$

where L_1 and L_2 are the self-inductance values.

Additionally, the substrate losses for the inner and outer windings were calculated separately by determining the admittance difference between two cases: a single inductor with and without the substrate. As expected, the outer inductor exhibited higher self-inductance, self-capacitance, and series-resistance values (Table II). A distance close to 30 µm between the two windings resulted in a coupling coefficient of $k = 0.47$, close to the theoretical limit of 0.5 for the concentric transformers.

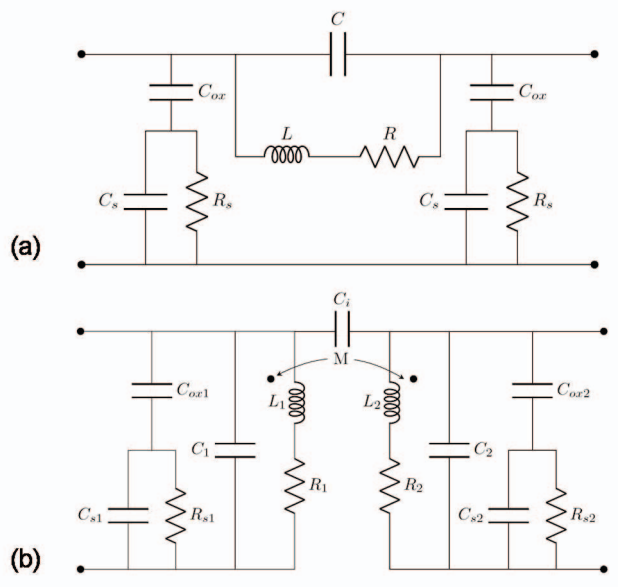

Fig. 3. Lumped-element models for: (a) the two-port planar inductor; and (b) the two-port planar transformer model on lossy substrates.

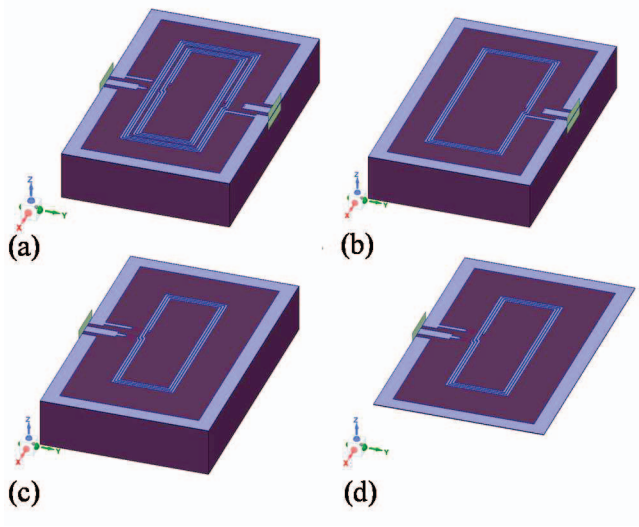

Fig. 4. HFSS simulation for electrical parameter extraction: (a) complete planar transformer with both windings, (b) external winding only, (c) internal winding only, and (d) internal winding only without the substrate.

TABLE II. LUMPED-ELEMENT VALUES FOR THE STUDIED CONCENTRIC TRANSFORMER.

Winding	Lumped-element values
Inner inductor	L_1 (23.7 nH), R_1 (22.9 Ω), C_1 (0.21 pF), C_{ox1} (160 pF), R_{s1} (0.92 Ω), C_{s1} (0.15 pF)
Outer inductor	L_2 (28.8 nH), R_2 (26.6 Ω), C_2 (0.31 pF), C_{ox2} (274 pF), R_{s2} (0.32 Ω), C_{s2} (0.2 pF)
Intertwining	M (13.2 nH), Ci (0.38 pF), k (0.47)

V. SENSITIVITY ESTIMATION

After establishing the relationship between the applied acceleration and the rotation angle between the transformer coils, the impact of this rotation on the magnetic coupling was investigated. Considering that an in-plane acceleration of 8 g resulted in a rotation of 5°, we analyzed several transformer structures with interwinding rotations ranging from 0° to 5° using HFSS (Fig. 5a). The results were analyzed and compared based on the mutual inductance values calculated at 100 MHz (Fig. 5b). As expected, the rotation resulted in a reduction in the mutual inductance due to the increase in the average distance between the parallel metal tracks of the two windings. From the neutral position to a 5° angle, the M value decreased from 13.86 nH to 12.8 nH, a change of 7.5%.

The extraction of the sensor electrical network parameters allowed us to study its interaction with a measurement circuit. We imported the S-parameters calculated for various acceleration inputs into Keysight ADS software, where the behavior of the sensor electrical network is used to emulate the measurement circuit. Fig. 6 illustrates the circuit implemented in ADS, which includes the sensor's S-parameter package, the output impedance of the signal generator (50 Ω), the parasitic capacitance of the wires (10 pF), and the input impedance (1 MΩ) of a read-out measurement setup such as an oscilloscope.

After exciting the circuit with a 3 V_{pp} AC signal at 100 MHz, the induced voltage measured on the 1 MΩ load

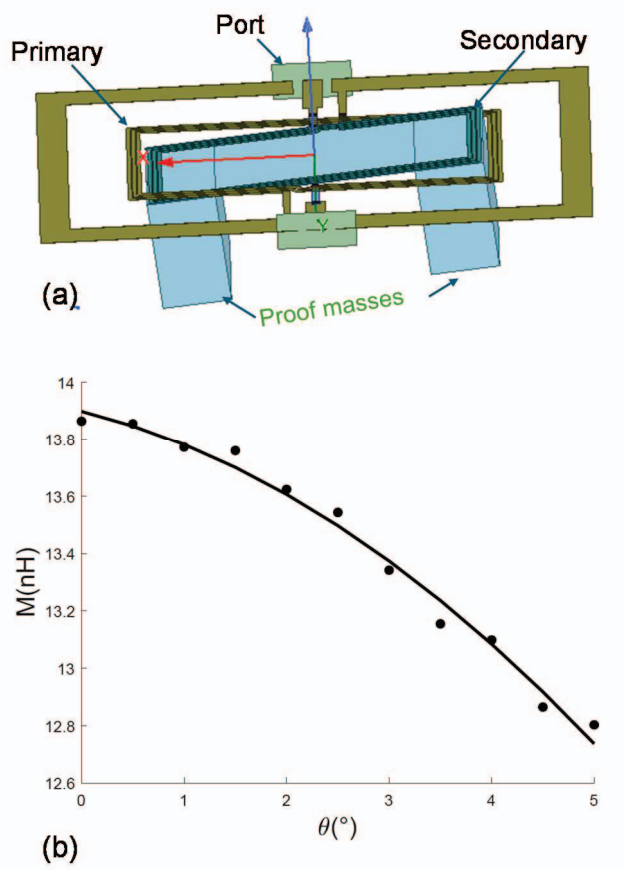

Fig. 5. (a) Overview of the HFSS simulation setup for off-plane rotation; (b) mutual inductance vs. angular displacement: individual simulation results (dots) and their 2nd degree polynomial fit (line).

was determined to be 0.306 V_{pp} at rest and 0.283 V_{pp} at 5° rotation under an acceleration of 8g. This corresponds to a sensitivity of 2.9 mV/g for the specified configuration. The sensitivity could be further improved by focusing on impedance matching around the measurement circuit. Already knowing the Z_{11} and Z_{22} impedances of the sensor from the S-parameter files, we used the Smith chart utility of the ADS software to match the source and load impedances around the sensor. This modification reduces the reflected waves within the circuit and improves the output response. From the rest state to 8g acceleration, the output voltage V_{out} decreased from 3.298 V peak-to-peak to 3.035 V. It corresponds to a sensitivity of 32.9 mV/g, demonstrating a ten-fold improvement over an unmatched circuit.

In practical applications, achieving a perfect impedance match might not be possible. However, this highlights the importance of the measurement setup for the sensors operating at RF frequencies. By pre-modeling the

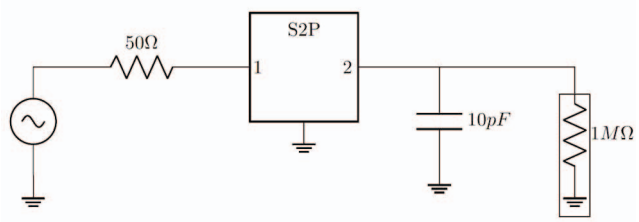

Fig. 6. ADS modelling the electromagnetic induction of the sensor in a measurement setup.

measurement setup in this way, circuit designers can plan their matching networks in advance and simplify the design cycle.

VI. Conclusions

A novel electromagnetic accelerometer design is presented in this work, which detects the in-plane acceleration through the changing magnetic coupling of a concentric transformer induced by the rotation between its primary and secondary windings. The proposed mechanical model was analytically studied to explain how the combined effect of plate bending and beam torsion is responsible for the rotation between the windings. COMSOL was then used to optimize the proof mass length to improve acceleration sensitivity. Once the geometry was finalized, the sensor body was subjected to the in-plane acceleration in order to calculate the resulting rotation. Electromagnetic simulations for these rotation values were performed in HFSS, with the results expressed in terms of the variation of the mutual inductance. Finally, the sensor was analyzed as a part of a measurement circuit in ADS with the previously extracted network parameters. With appropriate impedance matching, the electromagnetic accelerometer achieved an in-plane acceleration sensitivity of 32.9 mV/g when excited with $V_s=3V_{pp}$ at 100 MHz. This value is comparable to that of some commercial accelerometers on the market, highlighting the potential of the design and encouraging further investigation. Furthermore, the presented simulation flow provides future designers with a guideline for the systematic multiphysics analysis of sensors within the same electromagnetic sensor family.

Acknowledgments

This work was supported by the Scientific and Technological Research Council of Türkiye (TUBITAK) grant number 122E572. Professor Murat Kaya Yapici appreciates the support of the Turkish Academy of Sciences (TUBA) within the framework of the TUBA Outstanding Young Scientist Award Program (GEBIP'21); the Science Academy for the Young Scientist Award Program (BAGEP'23); and Elginkan Vakfi for the Technology Prize'24.

References

[1] Du S., "A micro-electro-mechanical-system-based inertial system with rotating accelerometers and gyroscopes for land vehicle navigation", Int. J. Distrib. Sens. N., 13 (12), pp. 1-10, Dec. 2017.

[2] D. Hyun Park, S. Shin, and Y. K. Kim, "Module packaging effects on MEMS airbag sensor performance for automobiles", Microelectron. Reliab., 79, 328-335, July 2017.

[3] F. Shemansky, Lj. Ristic, D. Koury and E. Joseph, "A two-chip accelerometer system for automotive applications", Microsyst. Technol., 1 (3), 121-123, July 1995.

[4] Kavitha S., Daniel R.J., and Sumangal K., "Design and Analysis of MEMS Comb Drive Capacitive Accelerometer for SHM and Seismic Applications", Measurement, 93, pp. 327-339, Nov. 2016.

[5] K. Wang, S. Lian and Z. Liu, "An Intelligent Screen System for Context-Related Scenery Viewing in Smart Home", IEEE Transactions on Consumer Electronics, 61 (1), February 2015.

[6] S. Du, "A micro-electro-mechanical-system-based inertial system with rotating accelerometers and gyroscopes for land vehicle navigation", Int. J. Distrib. Sens. N., 13 (12), 1-10, December 2017.

[7] V. B. Larin and A. A. Tunik, "On Inertial-Navigation System without Angular-Rate Sensors", Int. Appl. Mech. Journal, 49 (4), 488-499, July 2013.

[8] W. Wu, Z. Li, J. Liu, J. Fan, ve L. Tu. "A Nano-g MEMS Accelerometer for Earthquake Monitoring," 19th International Conference on Solid-State Sensors, Actuators and Microsystems, 2017.

[9] X. Zou, P. Thiruvenkatanathan, and A. A. Seshia. " A Seismic-Grade Resonant MEMS Accelerometer." J. of Microelectromech. Syst. 23, no. 4, 768–770, August 2014.

[10] A. Mustafazade, M. Pandit, C. Zhao, G. Sobreviela, Z. Du, P. Steinmann, X. Zou, R. T. Howe, and A. A. Seshia. "A Vibrating Beam MEMS Accelerometer for Gravity and Seismic Measurements," Scientific Reports 10, no. 1, June, 2020.

[11] B. Mezghani, F. Tounsi, and M. Masmoudi, "Convection behavior analysis of CMOS MEMS thermal accelerometers using FEM and Hardee's model," Analog Integrated Circuits and Signal Processing, vol. 78, pp. 301–311, 2014.

[12] Chau, Kevin H-L., and Robert E. Sulouff Jr. "Technology for the high-volume manufacturing of integrated surface-micromachined accelerometer products," Microelectronics Journal 29.9, pp. 579-586, 1998.

[13] A. Partridge, J.K. Reynolds, B.W. Chui, E.M. Chow, A.M. Fitzgerald, L. Zhang, N.I. Maluf, and T.W. Kenny "A high-performance planar piezoresistive accelerometer."Journal of microelectromechanical systems, vol. 9(1), pp. 58-66, 2000.

[14] L.P. Wang, R.A. Wolf, J.Y. Wang, K.K. Deng, L. Zou, R.J. Davis, and S. Trolier-McKinstry "Design, fabrication, and measurement of high-sensitivity piezoelectric microelectromechanical systems accelerometers," J. microelectromech. Syst., vol. 12(4), pp. 433-439, 2003.

[15] Abbaspour-Sani E., Huang R-S., and Kwok C.Y., "A linear electromagnetic accelerometer," Sensor. Actuat. A-Phys., vol. 44 (2), pp. 103-109, 1994.

[16] F. Tounsi, B. Mezghani, L. Rufer, S. Mir, and M. Masmoudi, "Electromagnetic modeling of an integrated micromachined inductive microphone," 4th International Conference on Design & Technology of Integrated Systems in Nanoscal Era, April 2009.

[17] Liu, Chang. "Foundations of MEMS", Pearson Education India, 2012.

[18] W.N. Sharpe Jr., J. Pulskamp, D.S. Gianola, C. Eberl, R.G. Polcawich and R.J. Thompson "Strain measurements of silicon dioxide microspecimens by digital imaging processing," *Exp. Mech., vol.* 47, 649-658, 2007.

[19] Hatty, Veronica, Harold Kahn, and Arthur H. Heuer. "Fracture toughness, fracture strength, and stress corrosion cracking of silicon dioxide thin films." J. microelectromech.systems, vol. 17(4), pp. 943-947, 2008.

[20] N. Zeidi, M. Rack, N. André, J.P. Raskin, F. Tounsi, and D. Flandre "Effect of Silicon Substrate Resistivity on Large-Area High Voltage Spiral Inductor Performance," IEEE Symposium on Design, Test, Integration & Packaging of MEMS/MOEMS (DTIP), 2023.

[21] Sunderarajan Sunderesan M., "The design, modeling and optimization of on-chip inductor and transformer circuits", Stanford University, 2000.